Clim. Past Discuss., 10, 2857–2893, 2014
www.clim-past-discuss.net/10/2857/2014/
doi:10.5194/cpd-10-2857-2014

Climate of the Past Discussions
Open Access

Carbon isotopes support Atlantic meridional overturning circulation decline as a trigger for early deglacial CO_2 rise

A. Schmittner[1] and D. C. Lund[2]

[1]College of Earth, Ocean, and Atmospheric Sciences, Oregon State University, Corvallis, Oregon, USA
[2]Department of Marine Sciences, University of Connecticut, USA

Received: 12 June 2014 – Accepted: 24 June 2014 – Published: 9 July 2014

Correspondence to: A. Schmittner (aschmitt@coas.oregonstate.edu)

Published by Copernicus Publications on behalf of the European Geosciences Union.

Abstract

The mechanism for the observed initial rise of atmospheric CO_2 during the last deglaciation remains unknown. Most recent hypotheses invoke Southern Hemisphere processes such as shifts in mid-latitude westerly winds. Here we compare simulations from a global, coupled climate-biogeochemistry model including carbon isotopes ($\delta^{13}C$) with a synthesis of high-resolution deep sea $\delta^{13}C$ reconstructions as well as ice core data. The reconstructions from Heinrich Stadial Event 1 (HS1, ~ 19–15 ka BP) are constistent with model simulations of a large multi-millennial reduction of the Atlantic Meridional Overturning Circulation (AMOC). Our results suggest that the rise in atmospheric CO_2 and decrease in its $\delta^{13}C$ composition ($\delta^{13}C_{CO_2}$) observed during the early deglacial may have been caused by an AMOC induced decline of the ocean's biologically sequestered carbon storage without the need to invoke changes in Southern Hemisphere winds.

1 Introduction

Earth's transition from the Last Glacial Maximum (LGM), 23–19 ka BP (thousand years before the present), into the modern warm period of the Holocene (10–0 ka BP) remains enigmatic (Denton et al., 2006). Evidence of early warming of the Southern Hemisphere and atmospheric CO_2 increase (Petit et al., 1999; Denton et al., 2010) has prompted hypotheses of a Southern Hemisphere trigger for the deglaciation (Stott et al., 2007; Timmermann et al., 2009). But the rise in atmospheric CO_2, although an important forcing for deglacial global warming (Shakun et al., 2012), remains unexplained. Various mechanisms have been proposed. Prominent recent studies suggest wind changes in the Southern Ocean (Anderson et al., 2009; Tschumi et al., 2011; Denton et al., 2010; Toggweiler et al., 2006) or changes in the North Pacific circulation (Menviel et al., 2014).

CPD
10, 2857–2893, 2014

Others have suggested that the deglaciation was initiated by a collapse of the AMOC caused by melting of Northern Hemisphere ice sheets (Denton et al., 2010; He et al., 2013; Shakun et al., 2012; Clark et al., 2004) and abrupt North Atlantic climate changes (Broecker et al., 1985). This idea has appeal since the AMOC is known from theory to exhibit multiple steady states with the possibility of rapid transitions between them (Stommel, 1961). Moreover, AMOC variations are consistent with the observed antiphasing of surface temperatures between the hemispheres (Schmittner et al., 2003; Shakun et al., 2012), evidence for ITCZ migration (Menviel et al., 2008), and atmospheric CO_2 increase (Schmittner and Galbraith, 2008). However, surface temperatures, rainfall patterns, and atmospheric gas concentrations alone do not allow robust inferences on the AMOC (Kurahashi-Nakamura et al., 2014) and evidence from the deep ocean for deglacial circulation variations remains sparse. One widely cited record of Protactinium-Thorium ratios ($^{231}Pa/^{320}Th$) from the subtropical North Atlantic has been interpreted as AMOC collapse around 19–18 ka BP followed by a rapid resumption $\sim$ 15 ka BP into the warm Boelling/Allerod period (McManus et al., 2004). However, this interpretation has been questioned (Keigwin and Boyle, 2008) and a subsequent set of $^{231}Pa/^{320}Th$ records (Gherardi et al., 2005) suggested that a complete AMOC cessation during HS1 was unlikely. Moreover, our understanding of $^{231}Pa/^{230}Th$ in the modern ocean continues to evolve (Anderson and Hayes, 2013) and inferences on the basin or global scale circulation from a single site require validation with multiple proxies from a range of oceanographic locations.

Deep sea $\delta^{13}C$ reconstructions are more common and the processes governing $\delta^{13}C$ are better understood (Schmittner et al., 2013). Here we compile deep ocean $\delta^{13}C$ reconstructions from the early deglacial and compare them with model simulations of $\delta^{13}C$ changes caused by AMOC variations in order to test the hypothesis that the AMOC was reduced during HS1. We also compare our model results to observations of atmospheric CO_2 concentrations and its $\delta^{13}C$ values in order to assess mechanisms of the early deglacial CO_2 rise.

CPD
10, 2857–2893, 2014

2 Methods

We have compiled 21 published deep ocean records covering the early deglacial at high temporal resolution (Table 1). Mostly published age models are used, which may have considerable (O(1 ka)) uncertainties. However, we believe that the records are of sufficient resolution and their age models are well enough constrained to evaluate multi-millennial changes. The purpose of this paper is to present an initial comparison to model results focusing on model analysis. Quantification of age uncertainties and their effects on the results are beyond the scope of this paper.

We employ the Model of Ocean Biogeochemistry and Isotopes (MOBI 1.4), a coupled climate-biogeochemical system that includes $\delta^{13}C$ cycling in the three-dimensional ocean, land, and atmosphere to explore the effect of AMOC variations on $\delta^{13}C$ cycling (see appendix for a more detailed model description). MOBI's large-scale ocean distribution of $\delta^{13}C_{DIC}$ in dissolved inorganic carbon (DIC) is consistent with modern water column observations (Schmittner et al., 2013). It is embedded in the University of Victoria climate model of intermediate complexity version 2.9 and run into a *pre-industrial* equilibrium with prognostic atmospheric CO_2 and $\delta^{13}C_{CO_2}$. Subsequently four numerical experiments, each $\sim$ 3500 years long, have been conducted with varying amplitudes (0.05 Sv, 0.1 Sv, 0.15 Sv, and 0.2 Sv; referred to as FW0.05, FW0.1, FW0.15, and FW0.2, respectively; Sv = Sverdrup = 10^6 m^3 s^{-1}) of a stepwise, 400 year long freshwater input to the North Atlantic (Fig. 1a). Note that these are idealized experiments, designed to examine only how AMOC variations impact the global $\delta^{13}C$ distribution. Realistic initial conditions for the LGM are currently not available. Thus, we do not attempt realistic deglacial simulations. However, it is well known that the $\delta^{13}C$ distribution of the LGM ocean (Curry and Oppo, 2005; Gebbie, 2014) and atmospheric CO_2 concentrations (Parrenin et al., 2013; Monnin et al., 2001; Lourantou et al., 2010) were different from the pre-industrial. In order to account for these differences in initial conditions our data-model comparison focuses on anomalies rather than absolute values.

CPD
10, 2857–2893, 2014

3 Results

3.1 Simulated carbon cycle changes

The AMOC reduces in all experiments (Fig. 1b). However, in FW0.05 and FW0.1 the reduction is reversible and after hosing is stopped the AMOC quickly returns to its initial state with negligible effects on atmospheric CO_2 (Fig. 1c). In experiments FW0.15 and FW0.2, on the other hand, the AMOC collapses permanently and CO_2 starts to increase about 500 years after the start of the hosing. CO_2 continues to increase gradually by ~ 25 ppm until year 2000, after which its rate of change slows. The amplitude and rate of change of the simulated CO_2 increase agrees well with measurements of early deglacial air recovered from Antarctic ice (Parrenin et al., 2013).

The simulated atmospheric CO_2 increase in FW0.15 and FW0.2 is due to a release of biologically sequestered carbon from the deep ocean (Figs. 2 and 3) consistent with previous results and theory (Schmittner and Galbraith, 2008; Ito and Follows, 2005; Marinov et al., 2008a, b). Initially Net Primary Production (NPP) declines within a few hundred years from 64 Gt C yr^{-1} to 54 Gt C yr^{-1} consistent with Schmittner (2005, not shown), which reduces the production of dissolved organic carbon (DOC), whereas dissolved inorganic carbon increases initially until around year 600, after which it starts to decline. By model year 3500 the ocean has lost ~ 120 Pg C (Fig. 2d) in FW0.15 most of which (~ 90 Pg C) due to DIC, and less (~ 30 Pg C) due to DOC. The ocean's DIC loss is caused by a reduced efficiency of the biological pump as indicated by the large loss of remineralized DIC (~ 400 Pg C; Fig. 2g) most of which is due to less organic matter oxidation (DIC_{org}; Fig. 3), whereas it is buffered by the increase in preformed DIC due to rising surface ocean DIC and atmospheric CO_2.

3.2 Simulated carbon isotope changes

Because biologically sequestered, organic carbon is isotopically light ($\delta^{13}C_{org} = -20$‰) its loss increases deep ocean $\delta^{13}C_{DIC}$ by ~ 0.06‰ (Fig. 2f) and decreases

CPD
10, 2857–2893, 2014

$\delta^{13}C_{DIC}$ (by ~ -0.3 ‰) in the surface ocean and $\delta^{13}C_{CO_2}$ by ~ -0.25 ‰ in the atmosphere (Fig. 1d). Modeled land carbon storage increases (Fig. 2a) and its average $\delta^{13}C_L$ decreases (Fig. 2c), implying that land cannot be the cause of the atmospheric changes. The simulated atmospheric $\delta^{13}C_{CO_2}$ decline in models FW0.15 and FW0.2 is consistent, both in amplitude and rate of change, with ice core measurements (Fig. 1d; Schmitt et al., 2012).

The simulated pre-industrial (model year 0; Fig. 4a–c) distribution of $\delta^{13}C_{DIC}$ in the ocean is characterized by high values in the surface and deep North Atlantic and low values in the deep North Pacific, consistent with a previous model version and observations (Schmittner et al., 2013). Sinking of well equilibrated surface waters causes high values in the deep North Atlantic, whereas aging and accumulation of isotopically light respired organic matter progressively decreases $\delta^{13}C_{DIC}$ as deep waters flow into the South Atlantic, and further into the Indian and Pacific Oceans. Thus, the modern interbasin difference in deep water $\delta^{13}C_{DIC}$ is caused by the interbasin MOC. Hence, as the AMOC collapses, the $\delta^{13}C_{DIC}$ difference between North Atlantic and North Pacific deep waters is reduced (Fig. 4d–f).

Differences between years 2500 and 0 (Fig. 4g–i) show the largest $\delta^{13}C_{DIC}$ decreases at intermediate depths (1–2.5 km) in the northern North Atlantic. Anomalies decrease further south but a pronounced minimum emerges at the depth of North Atlantic Deep Water (NADW; 2–3 km) in the South Atlantic with positive anomalies below, at the depth of Antarctic Bottom Water, and above, at the depth of Antarctic Intermediate Water. South of 40° S in the Atlantic as well as in the Indian and Pacific oceans $\delta^{13}C_{DIC}$ increases everywhere below ~ 500 m due to reduced export of ^{13}C-depleted carbon from the photic zone. Weakening of the biological pump causes surface ocean $\delta^{13}C$ to decrease by 0.2–0.4 ‰ in the Indian and Pacific basins, possibly explaining planktonic $\delta^{13}C$ minima on glacial terminations (Spero and Lea, 2002). The deep ocean signal dominates the global mean $\delta^{13}C_{DIC}$ increase of 0.04 ‰ by year 2500 (Fig. 2f). In the North Pacific $\delta^{13}C_{DIC}$ shows the largest increase around 1 km depth owing to reduced stratification and intensified intermediate water formation, which de-

CPD
10, 2857–2893, 2014

creases the amount of respired carbon there. Although changes in remineralized $\delta^{13}C$ ($\delta^{13}C_{rem}$; Fig. 5) dominate the spatial variations of the total $\delta^{13}C_{DIC}$ changes, preformed $\delta^{13}C$ ($\delta^{13}C_{pre}$) variations are not negligible, particularly in the Atlantic.

3.3 Observed carbon isotope changes during HS1

Observations from the North Atlantic show large $\delta^{13}C_{DIC}$ decreases early in the deglaciation (Fig. 6a–e; Fig. 7a). The largest amplitudes (~ -1 ‰) are found in high-resolution records from the northern North Atlantic (61° N) at intermediate (1.3–1.6 km) depths (Praetorius et al., 2008; Rickaby and Elderfield, 2005; Thornalley et al., 2010). Further south and in deeper water the $\delta^{13}C_{DIC}$ decrease is smaller (-0.4 to -0.7 ‰) (Vidal et al., 1997; Hodell et al., 2010; Zahn et al., 1997; Skinner and Shackleton, 2004; Labeyrie et al., 2005; Zahn and Stuber, 2002). Changes simulated at the same locations by model experiments FW0.15 and FW0.2, which exhibit multi-millennial AMOC collapses, are generally similar in amplitude, albeit somewhat larger. Despite similar AMOC evolutions model FW0.15 shows smaller amplitudes than model FW0.2, in better agreement with the reconstructions illustrating the local effect of the freshwater forcing. The overall spatial distribution of the observed $\delta^{13}C_{DIC}$ changes, with largest amplitudes at intermediate depths in the northern North Atlantic and decreasing further south and in deeper waters, is in best agreement with the results from model FW0.15 (Figs. 6 and 7; Table 2).

A new dataset from the Brazil Margin in the South Atlantic (Fig. 6f–k; Fig. 8) (Tessin and Lund, 2013; Lund et al., 2014) shows increasing $\delta^{13}C_{DIC}$ by ~ 0.35 ‰ at 1.1 km depth and decreasing $\delta^{13}C_{DIC}$ by ~ 0.5 ‰ between 1.6 and 2.1 km depth, whereas deeper in the water column the data are noisier without a clear trend. Model FW0.15's initial $\delta^{13}C_{DIC}$ values at the Brazil Margin are higher than the observations' mainly for two reasons (Fig. 8). First, the model does not consider the whole ocean lowering of $\delta^{13}C_{DIC}$ due to the reduction in land carbon during the LGM and second, it does not include the shoaling of NADW and very low $\delta^{13}C_{DIC}$ values in South Atlantic

CPD
10, 2857–2893, 2014

bottom waters (Curry and Oppo, 2005; Gebbie, 2014). Thus the simulated $\delta^{13}C_{DIC}$ decrease extends deeper than in the observations and shows a substantial reduction below 2.2 km. However, the reconstructed pattern of opposing $\delta^{13}C$ signal between shallow-intermediate and mid-depths agrees well with the simulated changes due to large AMOC reduction (Fig. 8). The rapid initial increase at intermediate depths appears to be influenced by two factors. First, reduced return flow of low $\delta^{13}C_{DIC}$ from the Indian ocean (not shown). Second, less upwelling of low $\delta^{13}C_{DIC}$ deep water into the upper and surface Southern Ocean leads to a deepening of the high $\delta^{13}C_{DIC}$ Antarctic Intermediate and Subantarctic Mode Waters, which, together with decreased stratification and deeper mixed layers (Schmittner et al., 2007a), increases $\delta^{13}C_{DIC}$ by ~ 0.3 ‰ at 1.2 km depth in all ocean basins at mid southern latitudes (Fig. 4g–i).

The simulated $\delta^{13}C_{DIC}$ increase at 1.2 km depth in the southwest Pacific (~ 0.5 ‰) and at 1.6 km depth in the tropical Indian Ocean (~ 0.3 ‰) agree well with local reconstructions (Fig. 6p and o). In deep waters of the Southern and Indian Oceans the reconstructions are noisy and no clear trend can be identified (Fig. 6l–n).

3.4 Sensitivity to wind changes

The model results discussed above did not include the effects of wind changes. Winds enter the UVic model in three ways:

1. Moisture advection velocities u_q determine convergence of specific humidity and thus precipitation.
2. Wind stress τ supplies momentum to the surface ocean and sea ice.
3. Wind speed u modulates air–sea exchange of heat, water, and gases (CO_2, O_2).

Fig. 10 shows the annual mean fields derived from the NCEP reanalysis (Kalnay et al., 1996) used in the above runs.

CPD
10, 2857–2893, 2014

In order to test the sensitivity of our results to these variables we performed three additional simulations, in which we use anomalies calculated from hosing experiments with the OSUVic model (bottom panels in Fig. 10). The OSUVic model includes a fully coupled dynamical atmosphere at T42 resolution (Schmittner et al., 2011), whereas the other components are identical to the UVic model version 2.8 without dynamic vegetation. In response to an AMOC shutdown OSUVic simulates a large anticyclonic anomaly over the North Atlantic, a cyclonic anomaly over the North Pacific, a southward shift of the Intertropical Convergence Zone (ITCZ) particularly over the Atlantic, and a southward shift of Southern Hemisphere westerlies consistent with previous studies (Timmermann et al., 2007; Zhang and Delworth, 2005; Schmittner et al., 2007b). Note that the changes in Southern Hemisphere westerlies are generally less than 10 % of the absolute values of the control simulation.

The OSUVic wind anomalies are applied at model year 400 of the FW0.15 simulation (blue dashed line in panel A of Fig. 11). The wind changes have only a modest impact on simulated carbon cycle and isotope distributions (Fig. 11). The larges effect is due to changes in moisture advection velocities, which lead to a rapid decrease in vegetation and soil carbon around year 400. This causes a rapid CO_2 increase by a few ppm and a rapid decrease of $\delta^{13}C_{CO_2}$ by a few hundredths of a permil. It also delays the oceanic carbon loss by a few hundred years. However, the multi-millennial response and our conclusions are not impacted much by the wind changes.

This is in contrast to the interpretation of Tschumi et al. (2011), who suggest Southern Ocean wind changes as the cause for the early deglacial CO_2 rise. However, in their idealized model experiments an 80 % increase in Southern Ocean winds leads to a drop of atmospheric $\delta^{13}C_{CO_2}$ by 0.2 ‰ (their Fig. 6). We think that such a large wind increase, similar to one expected from removing the entire Antarctic ice sheet (Schmittner et al., 2011), is unrealistic. General circulation models simulate much smaller changes (< 10 %) due to AMOC collapse (Fig. 10) (Schmittner et al., 2007b; Timmermann et al., 2007; Zhang and Delworth, 2005) or glacial boundary conditions (Otto-Bliesner et al., 2006; Brady et al., 2013).

CPD
10, 2857–2893, 2014

4 Discussion and conclusions

Taken together the deep ocean $\delta^{13}C_{DIC}$ reconstructions are consistent with a severe and prolonged, multi-millennial AMOC reduction during HS1. Model FW0.15 fits the reconstructions best as indicated by a high correlation coefficient ($r_{FW0.15} = 0.91$; Fig. 9; Table 2) and low root-mean-squared error ($rms_{FW0.15} = 0.40$). However, $\delta^{13}C_{DIC}$ changes in the North Atlantic are larger in the model than in the reconstructions. One reason for this discrepancy may be that AMOC changes during HS1 were smaller than those simulated (Gherardi et al., 2005; Lund et al., 2014). A second reason could be the mismatch in initial conditions. If the LGM AMOC was weaker and shallower than in the model's pre-industrial simulation as indicated by a number of reconstructions (Lynch-Stieglitz et al., 2007; Gebbie, 2014), the model would overestimate changes in volume fluxes and perhaps carbon isotopes even if a complete AMOC collapse occured during HS1. A third reason may be dampened records of the actual $\delta^{13}C_{DIC}$ changes by smoothing and averaging due to bioturbation, and/or age model errors. This may affect particularly low resolution sediment cores as indicated by reduced agreement with lower resolution data from a previous study (Sarnthein et al., 1994) ($r_{FW0.15} = 0.80$; $rms_{FW0.15} = 0.60$; Fig. 9). Resolving the likelihood of these different possibilities will be an important task for future research.

Our results support qualitatively McManus et al.'s (2004) interpretation of the $^{231}Pa/^{230}Th$ record, but more work is needed for an improved quantitative assessment. We suggest that an AMOC decline during HS1 could have caused the observed rise in atmospheric CO_2 and the decrease in $\delta^{13}C_{CO_2}$ by modulating the global efficiency of the ocean's biological pump. This is in contrast with ideas that invoke Southern Ocean (Anderson et al., 2009; Tschumi et al., 2011) and/or North Pacific (Menviel et al., 2014) mechanisms for the early deglacial CO_2 rise. If confirmed by future simulations with more realistic initial conditions and forcings, the deglacial mystery may shift towards its later stages, when the AMOC resumes but CO_2 keeps increasing, potentially related

CPD
10, 2857–2893, 2014

to the late deglacial rise in deep South Atlantic $\delta^{13}C_{DIC}$ (Lund et al., 2014), which will require a different mechanism from the one discussed here.

Appendix A: Model description

The University of Victoria Earth System Climate Model (UVic ESCM) (Weaver et al., 2001), is used in version 2.9 (Eby et al., 2009). It consists of a coarse resolution (1.8° × 3.6°, 19 vertical layers) ocean general circulation model coupled to a one layer atmospheric energy-moisture balance model and a dynamic thermodynamic sea ice model, both at the same horizontal resolution. The model is forced with seasonally varying solar irradiance at the top-of-the-atmosphere, cloud albedo, wind stress, wind speed, and moisture advection velocities. This seasonal forcing does not change between different years. Atmospheric CO_2 and $\delta^{13}C$ are calculated in a single box assuming rapid mixing.

A1 Description of land carbon isotopes ($\delta^{13}C$ and $\delta^{14}C$) model

The land carbon isotopes model has not been published before. Therefore we provide a description and evaluation here. It is based on TRIFFID, the "Top-down Representation of Interactive Foilage and Flora Including Dymamics" dynamic vegetation model by Cox (2001), as modified by Meissner et al. (2003) and Matthews et al. (2004), which solves prognostic equations for total vegetation carbon density $C_v = {}^{12}C_v + {}^{13}C_v$ and fractional coverage $v_i \in (0,1)$ of five plant functional types (PFTs; $i = 1,\ldots,5$):

$$\frac{\partial}{\partial t}\left(C_{v,i} v_i\right) = v_i \Pi_i - v_i \Lambda_i, \tag{A1}$$

CPD
10, 2857–2893, 2014

where Π_i is Net Primary Production (NPP) and Λ_i is litter production, which enters the soil carbon pool. Total soil carbon density is calculated according to

$$\frac{\partial}{\partial t} C_s = \sum_i \Lambda_i - R_s. \quad \text{(A2)}$$

We added prognostic equations for the heavy carbon isotopes ^{13}C and ^{14}C to both vegetation

$$\frac{\partial}{\partial t} \left({}^{13}C_{v,i} v_i \right) = \gamma^{13}_{\Pi,i} v_i \Pi_i - \gamma^{13}_{\Lambda,i} v_i \Lambda_i, \quad \text{(A3)}$$

and soil

$$\frac{\partial}{\partial t} {}^{13}C_s = \sum_i \gamma^{13}_{\Lambda,i} \Lambda_i - \gamma^{13}_R R_s, \quad \text{(A4)}$$

$$\frac{\partial}{\partial t} \left({}^{14}C_{v,i} v_i \right) = \gamma^{14}_{\Pi,i} v_i \Pi_i - \gamma^{14}_{\Lambda,i} v_i \Lambda_i - \kappa v_i {}^{14}C_{v,i}, \quad \text{(A5)}$$

and

$$\frac{\partial}{\partial t} {}^{14}C_s = \sum_i \lambda_{\Lambda,i} \Lambda_i - \gamma^{14}_R R_s - \kappa {}^{14}C_{s,\,i}, \quad \text{(A6)}$$

where fractionation during photosynthesis is indicated by factors

$$\gamma^{13}_{\Pi} = \frac{\beta^{13}_{\Pi}}{1 + \beta^{13}_{\Pi}}, \quad \text{(A7)}$$

and

$$\beta^{13}_{\Pi} = \alpha^{13}_{\Pi} R^{13}_A, \quad \text{(A8)}$$

CPD
10, 2857–2893, 2014

where

$$R_{\mathrm{A}}^{13} = \frac{{}^{13}\mathrm{C}_{\mathrm{CO}_2}}{{}^{12}\mathrm{C}_{\mathrm{CO}_2}} \tag{A9}$$

is the heavy to light isotope ratio of atmospheric CO_2.

Fractionation factors are different for C_3 and C_4 plants

$$\alpha_{\mathrm{NPP},i}^{13} = \begin{Bmatrix} 0.979, \text{ for } \mathrm{C}_3 \\ 0.993, \text{ for } \mathrm{C}_4 \end{Bmatrix}, \tag{A10}$$

which corresponds to a fractionation of $\varepsilon^{13} = (1 - \alpha^{13}) = -7‰$ for C_4 plants and $\varepsilon^{13} = -21‰$ for C_3 plants (O'Leary, 1988).

No fractionation occurs during litter production or respiration:

$$\gamma_{\Lambda}^{13} = \frac{\beta_{\Lambda}^{13}}{1 + \beta_{\Lambda}^{13}} \tag{A11}$$

$$\beta_{\Lambda}^{13} = R_{\mathrm{v},i}^{13} = \frac{{}^{13}\mathrm{C}_{\mathrm{v}}}{\mathrm{C}_{\mathrm{v}} - {}^{13}\mathrm{C}_{\mathrm{v}}} \tag{A12}$$

$$\gamma_{R}^{13} = \frac{\beta_{R}^{13}}{1 + \beta_{R}^{13}} \tag{A13}$$

$$\beta_{R}^{13} = R_{\mathrm{s}}^{13} = \frac{{}^{13}\mathrm{C}_{\mathrm{s}}}{\mathrm{C}_{\mathrm{s}} - {}^{13}\mathrm{C}_{\mathrm{s}}}. \tag{A14}$$

For radiocarbon Eqs. (A5) and (A6) radioactive decay is considered though $\kappa = 1.210 \times 10^{-4} a^{-1}$, which corresponds to a half life of 5730 years and twice the fractionation during NPP is assumed $\varepsilon^{14} = 2\varepsilon^{13}$, such that

$$\alpha_{\mathrm{NPP},i}^{14} = \begin{Bmatrix} 0.958, \text{for } \mathrm{C}_3 \\ 0.986, \text{for } \mathrm{C}_4 \end{Bmatrix}. \tag{A15}$$

CPD
10, 2857–2893, 2014

The simulated spatial distribution of average $\delta^{13}C$ (Fig. A1) varies from −13 ‰ in regions dominated by C_4 grasses such as North Africa and Australia to −27 ‰ in most other regions, which are dominated by C_3 plants, due to the differences in fractionation factors for C_3 and C_4 plants used in the model. This distribution is broadly consistent with previous independent estimates (Still and Powell, 2010; Powell et al., 2012).

A2 Description of ocean carbon isotope model

We use the Model of Ocean Biogeochemistry and Isotopes (MOBI) version 1.4. The ocean carbon isotope component is described in detail in Schmittner et al. (2013). Here we only describe differences with respect to that publication. The physical UVic model version was updated to version 2.9 (Schmittner et al., 2013 used 2.8). The ocean ecosystem model has been modified by changing zooplankton grazing, using a slightly different approach to consider iron limitation of phytoplankton growth as described in detail in (Keller et al., 2012). This model gives very similar results to model FeL in Schmittner et al. (2013).

Implementation of the carbon isotope equations have been changed from the "alpha" formulation to the "beta" formulation, courtesy of Chris Somes. In the "alpha" formulation the change in the heavy (rare) isotope carbon density ^{13}C (in mol C m^{-3}) of the product (e.g. phytoplankton) of some process (e.g. photosynthesis)

$$\frac{\partial}{\partial t}{}^{13}\mathrm{C} = \alpha R^{13}\frac{\partial}{\partial t}{}^{12}\mathrm{C} = \alpha R^{13}\frac{\partial}{\partial t}C, \tag{A16}$$

is calculated as the product of the total carbon change $\partial C/\partial t$ times the fractionation factor α for that process times the heavy to light isotope ratio of the source (e.g. sea water DIC) $R^{13} = {}^{13}C/{}^{12}\mathrm{C}$. This formulation assumes total carbon

$$C = {}^{12}\mathrm{C} + {}^{13}\mathrm{C} \approx {}^{12}\mathrm{C}, \tag{A17}$$

is equal to ^{12}C, which is a good approximation since ^{13}C is usually two orders of magnitude smaller than ^{12}C.

CPD
10, 2857–2893, 2014

However, assumption (A17) can be avoided by using the "beta" formulation, in which the heavy isotope change is calculated according to

$$\frac{\partial}{\partial t}{}^{13}\mathrm{C} = \frac{\beta^{13}}{1+\beta^{13}}\frac{\partial}{\partial t}\mathrm{C}, \tag{A18}$$

where $\beta^{13} = \alpha^{13}R^{13}$.

In order to convert isotope ratios to delta values

$$\delta^{13}\mathrm{C} = (R/R_{\mathrm{std}} - 1) \tag{A19}$$

we now use the conventional standard ratio $R^{13}_{\mathrm{std}} = 0.0112372$ instead of $R^{13}_{\mathrm{std}} = 1$, which was used in (Schmittner et al., 2013). For radiocarbon $R^{14}_{\mathrm{std}} = 1.17 \times 10^{-12}$ is used.

MOBI 1.4 includes dissolved organic carbon (DOC) cycling described in Somes et al. (2014). The close agreement of the preindustrial $\delta^{13}\mathrm{C}_{\mathrm{DIC}}$ distributions with model FeL of Schmittner et al. (2013) suggest that none of the changes described above have a major impact of the simulated $\delta^{13}\mathrm{C}_{\mathrm{DIC}}$.

Acknowledgements. AS has been supported by the National Science Foundation's Marine Geology and Geophysics program grant OCE-1131834. Most reconstructions listed in Table 2 were extracted from the National Oceanic and Atmospheric Administration's (NOAA) National Climatic Data Center (NCDC) Paleoclimatology Program Database (http://www.ncdc.noaa.gov/data-access/paleoclimatology-data). We are grateful to all data generators who make their data available on public databases. We are also thankful to Claire Waelbroeck, Rainer Zahn, and Ros Rickaby for generously sharing data used in this study. Thanks to Christopher Somes for re-writing the carbon isotope model in the "beta" formulation.

References

Anderson, R. and Hayes, C.: New insights into gochemical proxies from GEOTRACES, 11th International Conference on Paleoceanography, Sitges, Spain, 2013.

CPD
10, 2857–2893, 2014

Anderson, R. F., Ali, S., Bradtmiller, L. I., Nielsen, S. H. H., Fleisher, M. Q., Anderson, B. E., and Burckle, L. H.: Wind-driven upwelling in the Southern Ocean and the deglacial rise in atmospheric CO_2, Science, 323, 1443–1448, doi:10.1126/Science.1167441, 2009.

Brady, E. C., Otto-Bliesner, B. L., Kay, J. E., and Rosenbloom, N.: Sensitivity to glacial forcing in the CCSM4, J. Climate, 26, 1901–1925, doi:10.1175/jcli-d-11-00416.1, 2013.

Broecker, W. S., Peteet, D. M., and Rind, D.: Does the ocean–atmosphere system have more than one stable mode of operation?, Nature, 315, 21–26, 1985.

Charles, C. D., Lynch-Stieglitz, J., Ninnemann, U. S., and Fairbanks, R. G.: Climate connections between the hemisphere revealed by deep sea sediment core ice core correlations, Earth Planet. Sc. Lett., 142, 19–27, 1996.

Clark, P. U., McCabe, A. M., Mix, A. C., and Weaver, A. J.: Rapid rise of sea level 19 000 years ago and its global implications, Science, 304, 1141–1144, doi:10.1126/Science.1094449, 2004.

Cox, P.: Description of the "TRIFFID" Dynamic Global Vegetation Model, Hadley Center, Technical Note 24, 1–16, 2001.

Curry, W. B. and Oppo, D. W.: Glacial water mass geometry and the distribution of delta C-13 of Sigma CO_2 in the western Atlantic Ocean, Paleoceanography, 20, PA1017, doi:10.1029/2004PA001021, 2005.

Denton, G., Broecker, W. S., and Alley, R. B.: The mystery invervall 17.5 to 14.5 kyr ago, PAGES News, 14, 14–16, 2006.

Denton, G. H., Anderson, R. F., Toggweiler, J. R., Edwards, R. L., Schaefer, J. M., and Putnam, A. E.: The last glacial termination, Science, 328, 1652–1656, doi:10.1126/science.1184119, 2010.

Eby, M., Zickfeld, K., Montenegro, A., Archer, D., Meissner, K. J., and Weaver, A. J.: Lifetime of anthropogenic climate change: millennial time scales of potential CO_2 and surface temperature perturbations, J. Climate, 22, 2501–2511, doi:10.1175/2008jcli2554.1, 2009.

Gebbie, G.: How much did glacial North Atlantic water shoal?, Paleoceanography, 29, 190–209, doi:10.1002/2013PA002557, 2014.

Gherardi, J., Labeyrie, L., McManus, J., Francois, R., Skinner, L., and Cortijo, E.: Evidence from the Northeastern Atlantic basin for variability in the rate of the meridional overturning circulation through the last deglaciation, Earth Planet. Sc. Lett., 240, 710–723, doi:10.1016/j.epsl.2005.09.061, 2005.

CPD
10, 2857–2893, 2014

He, F., Shakun, J. D., Clark, P. U., Carlson, A. E., Liu, Z., Otto-Bliesner, B. L., and Kutzbach, J. E.: Northern Hemisphere forcing of Southern Hemisphere climate during the last deglaciation, Nature, 494, 81–85, doi:10.1038/nature11822, 2013.

Hodell, D. A., Evans, H. F., Channell, J. E. T., and Curtis, J. H.: Phase relationships of North Atlantic ice-rafted debris and surface-deep climate proxies during the last glacial period, Quaternary Sci. Rev., 29, 3875–3886, doi:10.1016/J.Quascirev.2010.09.006, 2010.

Ito, T. and Follows, M. J.: Preformed phosphate, soft tissue pump and atmospheric CO_2, J. Mar. Res., 63, 813–839, 2005.

Jung, S. J. A., Kroon, D., Ganssen, G., Peeters, F., and Ganeshram, R.: Enhanced Arabian Sea intermediate water flow during glacial North Atlantic cold phases, Earth Planet. Sc. Lett., 280, 220–228, 2009.

Kalnay, E., Kanamitsu, M., Kistler, R., Collins, W., Deaven, D., Gandin, L., Iredell, M., Saha, S., White, G., Woollen, J., Zhu, Y., Chelliah, M., Ebisuzaki, W., Higgins, W., Janowiak, J., Mo, K. C., Ropelewski, C., Wang, J., Leetmaa, A., Reynolds, R., Jenne, R., and Joseph, D.: The NCEP/NCAR 40 year reanalysis project, B. Am. Meteorol. Soc., 77, 437–471, 1996.

Keigwin, L. D. and Boyle, E. A.: Did North Atlantic overturning halt 17,000 years ago?, Paleoceanography, 23, PA1101, doi:10.1029/2007PA001500, 2008.

Keller, D. P., Oschlies, A., and Eby, M.: A new marine ecosystem model for the University of Victoria Earth System Climate Model, Geosci. Model Dev., 5, 1195–1220, doi:10.5194/gmd-5-1195-2012, 2012.

Kurahashi-Nakamura, T., Losch, M., and Paul, A.: Can sparse proxy data constrain the strength of the Atlantic meridional overturning circulation?, Geosci. Model Dev., 7, 419–432, doi:10.5194/gmd-7-419-2014, 2014.

Labeyrie, L., Waelbroeck, C., Cortijo, E., Michel, E., and Duplessy, J. C.: Changes in deep water hydrology during the Last Deglaciation, CR Geosci., 337, 919–927, doi:10.1016/J.Crte.2005.05.010, 2005.

Lourantou, A., Lavric, J. V., Kohler, P., Barnola, J. M., Paillard, D., Michel, E., Raynaud, D., and Chappellaz, J.: Constraint of the CO2 rise by new atmospheric carbon isotopic measurements during the last deglaciation, Global Biogeochem Cy, 24, GB2015, doi:10.1029/2009gb003545, 2010.

Lund, D. C., Tessin, A. C., Hoffman, J. L., and Schmittner, A.: Southwest Atlantic watermass evolution during the last deglaciation, Paleoceanography, submitted, 2014.

CPD
10, 2857–2893, 2014

Lynch-Stieglitz, J., Adkins, J. F., Curry, W. B., Dokken, T., Hall, I. R., Herguera, J. C., Hirschi, J. J. M., Ivanova, E. V., Kissel, C., Marchal, O., Marchitto, T. M., McCave, I. N., McManus, J. F., Mulitza, S., Ninnemann, U., Peeters, F., Yu, E. F., and Zahn, R.: Atlantic meridional overturning circulation during the Last Glacial Maximum, Science, 316, 66–69, doi:10.1126/Science.1137127, 2007.

Marinov, I., Follows, M., Gnanadesikan, A., Sarmiento, J. L., and Slater, R. D.: How does ocean biology affect atmospheric pCO_2? Theory and models, J. Geophys. Res., 113, C07032, doi:10.1029/2007jc004598, 2008a.

Marinov, I., Gnanadesikan, A., Sarmiento, J. L., Toggweiler, J. R., Follows, M., and Mignone, B. K.: Impact of oceanic circulation on biological carbon storage in the ocean and atmospheric pCO_2, Global Biogeochem. Cy., 22, GB3007, doi:10.1029/2007GB002958, 2008b.

Matthews, H. D., Weaver, A. J., Meissner, K. J., Gillett, N. P., and Eby, M.: Natural and anthropogenic climate change: incorporating historical land cover change, vegetation dynamics and the global carbon cycle, Clim. Dynam., 22, 461–479, doi:10.1007/s00382-004-0392-2, 2004.

McManus, J. F., Francois, R., Gherardi, J. M., Keigwin, L. D., and Brown-Leger, S.: Collapse and rapid resumption of Atlantic meridional circulation linked to deglacial climate changes, Nature, 428, 834–837, 2004.

Meissner, K. J., Weaver, A. J., Matthews, H. D., and Cox, P. M.: The role of land surface dynamics in glacial inception: a study with the UVic Earth System Model, Clim. Dynam., 21, 515–537, doi:10.1007/S00382-003-0352-2, 2003.

Menviel, L., Timmermann, A., Mouchet, A., and Timm, O.: Meridional reorganizations of marine and terrestrial productivity during Heinrich events, Paleoceanography, 23, PA1203, doi:10.1029/2007pa001445, 2008.

Menviel, L., England, M. H., Meissner, K. J., Mouchet, A., and Yu, J.: Atlantic-Pacific seesaw and its role in outgassing CO2 during Heinrich events, Paleoceanography, 29, 58–70, doi:10.1002/2013pa002542, 2014.

Monnin, E., Indermühle, A., Dällenbach, A., Flückiger, J., Stauffer, B., Stocker, T. F., Raynaud, D., and Barnola, J.-M.: Atmospheric CO_2 concentrations over the Last Glacial Termination, Science, 291, 112–114, doi:10.1126/science.291.5501.112, 2001.

O'Leary, M. H.: Carbon isotopes in photosynthesis, Bioscience, 38, 328–336, 1988.

CPD
10, 2857–2893, 2014

Otto-Bliesner, B. L., Brady, E. C., Clauzet, G., Tomas, R., Levis, S., and Kothavala, Z.: Last Glacial maximum and holocene climate in CCSM3, J. Climate, 19, 2526–2544, 2006.
Pahnke, K. and Zahn, R.: Southern Hemisphere water mass conversion linked with North Atlantic climate variability, Science, 307, 1741–1746, 2005.
Parrenin, F., Masson-Delmotte, V., Köhler, P., Raynaud, D., Paillard, D., Schwander, J., Barbante, C., Landais, A., Wegner, A., and Jouzel, J.: Synchronous change of atmospheric CO_2 and Antarctic temperature during the last deglacial warming, Science, 339, 1060–1063, doi:10.1126/science.1226368, 2013.
Petit, J. R., Jouzel, J., Raynaud, D., Barkov, N. I., Barnola, J. M., Basile, I., Bender, M., Chappellaz, J., Davis, M., Delaygue, G., Delmotte, M., Kotlyakov, V. M., Legrand, M., Lipenkov, V. Y., Lorius, C., Pepin, L., Ritz, C., Saltzman, E., and Stievenard, M.: Climate and atmospheric history of the past 420 000 years from the Vostok ice core, Antarctica, Nature, 399, 429–436, 1999.
Powell, R. L., Yoo, E.-H., and Still, C. J.: Vegetation and soil carbon-13 isoscapes for South America: integrating remote sensing and ecosystem isotope measurements, Ecosphere, 3, art109, doi:10.1890/ES12-00162.1, 2012.
Praetorius, S. K., McManus, J. F., Oppo, D. W., and Curry, W. B.: Episodic reductions in bottom-water currents since the last ice age, Nat Geosci, 1, 449–452, doi:10.1038/ngeo227, 2008.
Rickaby, R. E. M. and Elderfield, H.: Evidence from the high-latitude North Atlantic for variations in Antarctic intermediate water flow during the last deglaciation, Geochem. Geophy. Geosy., 6, Q05001, doi:10.1029/2004GC000858, 2005.
Sarnthein, M., Winn, K., Jung, S. J., Duplessy, J. C., Labeyrie, L., Erlenkeuser, H., and Ganssen, G.: Changes in east Atlantic deepwater circulation over the last 30 000 years: eight time slice reconstructions, Paleoceanography, 9, 209–267, 1994.
Schmitt, J., Schneider, R., Elsig, J., Leuenberger, D., Lourantou, A., Chappellaz, J., Köhler, P., Joos, F., Stocker, T. F., Leuenberger, M., and Fischer, H.: Carbon isotope constraints on the deglacial CO_2 rise from ice cores, Science, 336, 711–714, doi:10.1126/science.1217161, 2012.
Schmittner, A., Saenko, O. A., and Weaver, A. J.: Coupling of the hemispheres in observations and simulations of glacial climate change, Quaternary Sci. Rev., 22, 659–671, 2003.
Schmittner, A.: Decline of the marine ecosystem caused by a reduction in the Atlantic overturning circulation, Nature, 434, 628–633, 2005.

CPD
10, 2857–2893, 2014

Schmittner, A. and Galbraith, E. D.: Glacial greenhouse-gas fluctuations controlled by ocean circulation changes, Nature, 456, 373–376, doi:10.1038/nature07531, 2008.
Schmittner, A., Brook, E. J., and Ahn, J.: Impact of the ocean's overturning circulation on atmospheric CO_2, in: Ocean Circulation: Mechanisms and Impacts, edited by: Schmittner, A., Chiang, J. C. H., and Hemming, S. R., Geophysical Monograph Series, 173, American Geophysical Union, Washington DC, 315–334, 2007a.
Schmittner, A., Galbraith, E. D., Hostetler, S. W., Pedersen, T. F., and Zhang, R.: Large fluctuations of dissolved oxygen in the Indian and Pacific oceans during Dansgaard-Oeschger oscillations caused by variations of North Atlantic Deep Water subduction, Paleoceanography, 22, PA3207, doi:10.1029/2006PA001384, 2007b.
Schmittner, A., Silva, T. A., Fraedrich, K., Kirk, E., and Lunkeit, F.: Effects of mountains and ice sheets on global ocean circulation, J. Climate, 24, 2814–2829, doi:10.1175/2010JCLI3982.1, 2011.
Schmittner, A., Gruber, N., Mix, A. C., Key, R. M., Tagliabue, A., and Westberry, T. K.: Biology and air–sea gas exchange controls on the distribution of carbon isotope ratios ($\delta^{13}C$) in the ocean, Biogeosciences, 10, 5793–5816, doi:10.5194/bg-10-5793-2013, 2013.
Shakun, J. D., Clark, P. U., He, F., Marcott, S. A., Mix, A. C., Liu, Z. Y., Otto-Bliesner, B., Schmittner, A., and Bard, E.: Global warming preceded by increasing carbon dioxide concentrations during the last deglaciation, Nature, 484, 49–54, doi:10.1038/Nature10915, 2012.
Sirocko, F., Sarnthein, M., Erlenkeuser, H., Lange, H., Arnold, M., and Duplessy, J. C.: Century-scale events in monsoonal climate over the past 24,000 years, Nature, 364, 322–324, 1993.
Skinner, L. C. and Shackleton, N.: Rapid transient changes in Northeast Atlantic deep water ventilation age across termination I, Paleoceanography, 19, doi:10.1029/2003pa000983, 2004.
Spero, H. J. and Lea, D. W.: The cause of carbon isotope minimum events on glacial terminations, Science, 296, 522–525, doi:10.1126/Science.1069401, 2002.
Still, C. J. and Powell, R. L.: Continental-Scale Distributions of Vegetation Stable Carbon Isotope Ratios, in, edited by: West, J. B., Bowen, G. J., Dawson, T. E., and Tu, K. P., Springer Netherlands, Dordrecht, 179–193, 2010.
Stommel, H.: Thermohaline convection with two stable regimes of flow, Tellus, 13, 224–230, 1961.

CPD
10, 2857–2893, 2014

Stott, L., Timmermann, A., and Thunell, R.: Southern Hemisphere and deep-sea warming led deglacial atmospheric CO_2 rise and tropical warming, Science, 318, 435–438, doi:10.1126/Science.1143791, 2007.

Tessin, A. C. and Lund, D. C.: Isotopically depleted carbon in the mid-depth South Atlantic during the last deglaciation, Paleoceanography, 28, 296–306, doi:10.1002/palo.20026, 2013.

Thornalley, D. J. R., Elderfield, H., and McCave, I. N.: Intermediate and deep water paleoceanography of the northern North Atlantic over the past 21,000 years, Paleoceanography, 25, PA1211, doi:10.1029/2009pa001833, 2010.

Timmermann, A., Okumura, Y., An, S. I., Clement, A., Dong, B., Guilyardi, E., Hu, A., Jungclaus, J. H., Renold, M., Stocker, T. F., Stouffer, R. J., Sutton, R., Xie, S. P., and Yin, J.: The influence of a weakening of the Atlantic meridional overturning circulation on ENSO, J. Climate, 20, 4899–4919, doi:10.1175/Jcli4283.1, 2007.

Timmermann, A., Timm, O., Stott, L., and Menviel, L.: The roles of CO_2 and orbital forcing in driving Southern Hemispheric temperature variations during the Last 21 000 yr, J. Climate, 22, 1626–1640, doi:10.1175/2008jcli2161.1, 2009.

Toggweiler, J. R., Russell, J. L., and Carson, S. R.: Midlatitude westerlies, atmospheric CO_2, and climate change during the ice ages, Paleoceanography, 21, Pa2005, doi:10.1029/2005pa001154, 2006.

Tschumi, T., Joos, F., Gehlen, M., and Heinze, C.: Deep ocean ventilation, carbon isotopes, marine sedimentation and the deglacial CO_2 rise, Clim. Past, 7, 771–800, doi:10.5194/cp-7-771-2011, 2011.

Vidal, L., Labeyrie, L., Cortijo, E., Arnold, M., Duplessy, J. C., Michel, E., Becque, S., and vanWeering, T. C. E.: Evidence for changes in the North Atlantic Deep Water linked to meltwater surges during the Heinrich events, Earth Planet. Sc. Lett., 146, 13–27, doi:10.1016/S0012-821x(96)00192-6, 1997.

Waelbroeck, C., Skinner, L. C., Labeyrie, L., Duplessy, J. C., Michel, E., Vazquez Riveiros, N., Gherardi, J. M., and Dewilde, F.: The timing of deglacial circulation changes in the Atlantic, Paleoceanography, 26, PA3213, doi:10.1029/2010pa002007, 2011.

Weaver, A. J., Eby, M., Wiebe, E. C., Bitz, C. M., Duffy, P. B., Ewen, T. L., Fanning, A. F., Holland, M. M., MacFadyen, A., Matthews, H. D., Meissner, K. J., Saenko, O., Schmittner, A., Wang, H. X., and Yoshimori, M.: The UVic Earth System Climate Model: model description, climatology, and applications to past, present and future climates, Atmos. Ocean, 39, 361–428, 2001.

CPD
10, 2857–2893, 2014

Zahn, R. and Stuber, A.: Suborbital intermediate water variability inferred from paired benthic foraminiferal Cd/Ca and delta C-13 in the tropical West Atlantic and linking with North Atlantic climates, Earth Planet. Sc. Lett., 200, 191–205, doi:10.1016/S0012-821x(02)00613-1, 2002.

Zahn, R., Schonfeld, J., Kudrass, H. R., Park, M. H., Erlenkeuser, H., and Grootes, P.: Thermohaline instability in the North Atlantic during meltwater events: stable isotope and ice-rafted detritus records from core SO75-26KL, Portuguese margin, Paleoceanography, 12, 696–710, doi:10.1029/97pa00581, 1997.

Zhang, R. and Delworth, T. L.: Simulated tropical response to a substantial weakening of the Atlantic thermohaline circulation, J. Climate, 18, 1853–1860, doi:10.1175/Jcli3460.1, 2005.

Ziegler, M., Diz, P., Hall, I. R., and Zahn, R.: Millennial-scale changes in atmospheric CO2 levels linked to the Southern Ocean carbon isotope gradient and dust flux, Nat. Geosci., 6, 457–461, doi:10.1038/ngeo1782, 2013.

CPD
10, 2857–2893, 2014

Table 1. Sediment cores used in this study.

	Core	Longitude	Latitude	Depth (m)	References	Age Model (if different)
1	ODP984	61° N	24° W	1649	Praetorius et al. (2008)	
2	NEAP4K	61° N	24° W	1627	Rickaby and Elderfield (2005)	
3	RAPiD-10-1P	62° N	17° W	1237	Thornalley et al. (2010)	
4	NA87-22	55° N	14° W	2161	Vidal et al. (1997)	Waelbroeck et al. (2011)
5	KN166-14-JPC-13	53° N	33° W	3082	Hodell et al. (2010)	
6	SO75-26KL	37° N	10° W	1099	Zahn et al. (1997)	Waelbroeck et al. (2011)*
7	MD99-2334K	37° N	10° W	3146	Skinner and Shackleton (2004)	
8	MD95-2037	37° N	32° W	2159	Labeyrie et al. (2005)	Waelbroeck et al. (2011)
9	M35003-4	12° N	61° W	1299	Zahn and Stuber (2002)	Waelbroeck et al. (2011)
10	KNR159-5 90GGC	27° S	46° W	1105	Lund et al. (2012); Curry and Oppo (2005)	
11	KNR159-5 36GGC	27° S	46° W	1268	Tessin and Lund (2013)	
12	KNR159-5 17JPC	27° S	46° W	1627	Tessin and Lund (2013)	
13	KNR159-5 33GGC	27° S	46° W	2082	Tessin and Lund (2013)	
14	KNR159-5 42JPC	27° S	46° W	2296	Tessin and Lund (2013)	
15	KNR159-5 30GGC	27° S	46° W	2500	Tessin and Lund (2013)	
16	KNR159-5 125GGC	27° S	46° W	3589	Tessin and Lund (2013)	
17	RC11-83	41° S	9° E	4718	Charles et al. (1996)	
18	MD01-2588	41° S	25° E	2907	Ziegler et al. (2013)	
19	74KL	14° N	57° E	3,212	Sirocko et al. (1993)	
20	NIOP905	10° N	52° E	1580	Jung et al. (2009)	
21	MD97-2120	45° S	174° E	1210	Pahnke and Zahn (2005)	

* LGM was shifted 1.5 ka younger in order to be consistent with the timing of the other North Atlantic core's $\delta^{13}C$ decline.

CPD
10, 2857–2893, 2014

Table 2. Statistical indices of comparison for the reconstructed HS1 (15.5–16.5 ka BP) minus LGM (18.5–19.5 ka BP) ocean $\delta^{13}C$ changes with those from the model simulations (model year 2500 minus year −500). Correlation coefficients (r) and root-mean-squared errors (rms). The number of datapoints is $n = 21$.

Model	R	rms
FW0.05	0.77	0.48
FW0.1	0.77	0.47
FW0.15	0.91	0.40
FW0.2	0.90	0.53

CPD
10, 2857–2893, 2014

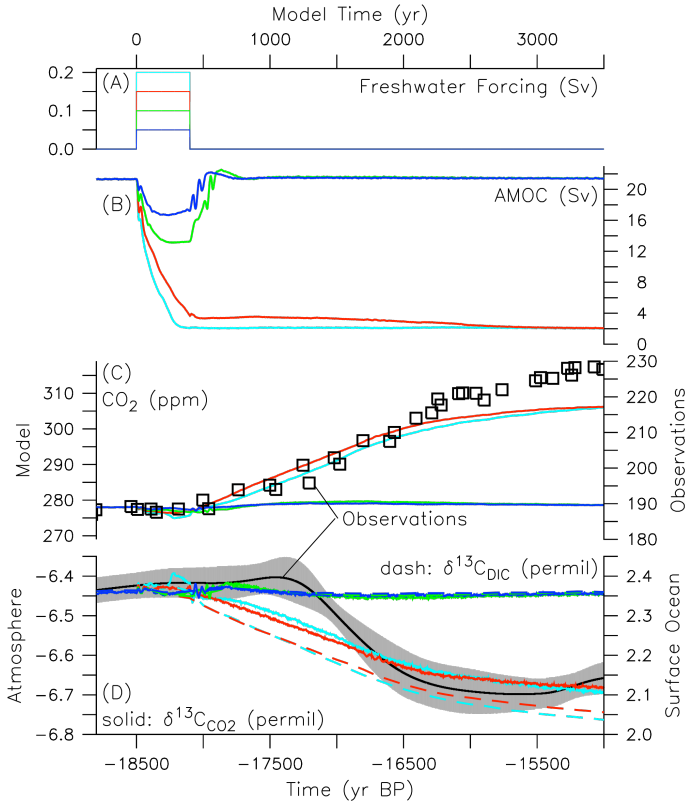

Figure 1. Time series of **(A)** North Atlantic freshwater forcing, **(B)** AMOC response, **(C)** atmospheric CO_2 concentrations, **(D)** $\delta^{13}C$ of atmospheric CO_2 (solid, left axis) and global mean surface ocean $\delta^{13}C_{DIC}$ (dashed, right axis) for four model simulations (color lines). Symbols in **(C)** and black curve (error estimates are shaded grey) in **(D)** show ice core measurements (Parrenin et al., 2013, 2012), respectively (bottom and right (in (C)) axes).

CPD
10, 2857–2893, 2014

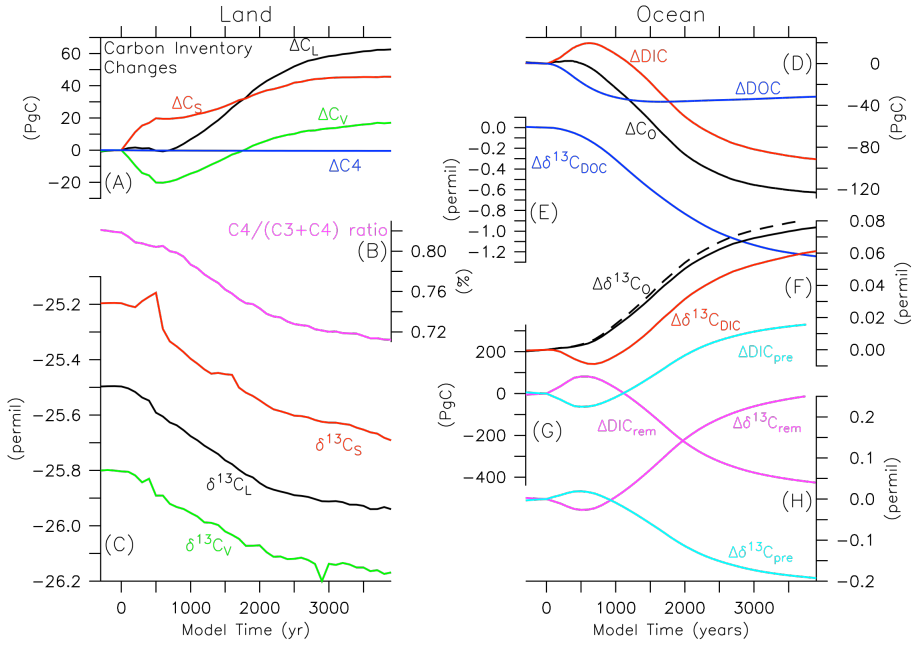

CPD
10, 2857–2893, 2014

AMOC triggers CO_2 rise

A. Schmittner and D. C. Lund

Figure 2. Simulated changes in global land (left) and ocean (right) carbon inventories (in Pg C; 1 ppm = 2.1 Pg C) and their averaged $\delta^{13}C$ (in permil) in model FW0.15. Changes in **(A)** land carbon $\Delta C_L = \Delta C_V + \Delta C_S$ (black) are due to vegetation ΔC_V (green) and soil ΔC_S (red) changes. Vegetation is composed of C_3 and C_4 plants, $C_V = C_3 + C_4$, but C_4 plants contribute only a small fraction **(B)** to the total. Changes in C_4 plant biomass (blue line in **A**) are negligible compared to those of C_3 plants (difference between green and blue lines). Panel **(C)** shows biomass weighted mean $\delta^{13}C$ of the land $\delta^{13}C_L = (\sum_i C_{v,i} \cdot \delta^{13}C_i + C_s \cdot \delta^{13}C_s)/(\sum_i C_{v,i} + C_s)$ (black), vegetation $\delta^{13}C_v = (\sum_i C_{v,i} \cdot \delta^{13}C_i)/(\sum_i C_{v,i})$ (green), and soil $\delta^{13}C_s$ (red). Ocean carbon changes $\Delta C_O = \Delta DIC + \Delta DOC \underbrace{+\Delta POC}_{\sim 0}$ (**D**, black) are due to dissolved organic (DOC, blue) and inorganic (DIC, red) carbon, and negligible changes in particulate organic carbon (POC, not shown). Total ocean $\delta^{13}C_O = (DIC \cdot \delta^{13}C_{DIC} + DOC \cdot \delta^{13}C_{DOC})/(DIC + DOC)$ (**F**, black) is dominated by changes in $\delta^{13}C_{DIC}$ (red). $\delta^{13}C_{DOC}$ (blue line in panel **E**) changes play only a minor role for $\Delta\delta^{13}C_O$ as illustrated by the dashed black line in **(F)**, which was calculated assuming a constant $\delta^{13}C_{DOC} = -21.5$ ‰. However, the relative contribution of DOC to C_O decreases by about 10 %, which explains the difference between the solid red and dashed black lines in **(F)**. DIC changes are further separated into remineralized (DIC_{rem}, $\Delta\delta^{13}C_{rem}$, purple) and preformed (DIC_{pre}, $\Delta\delta^{13}C_{pre}$, light blue) components in **(G)** and **(H)** following Schmittner et al. (2014). All anomalies are shown relative to model year 0, at which absolute numbers are $C_L = 1785$ Pg C, $C_O = 37390$ Pg C, $C_{DIC} = 37191$ Pg C, $C_{DOC} = 297$ Pg C, $C_{POC} = 2$ Pg C, $\delta^{13}C_{DIC} = 0.72$ ‰, $\delta^{13}C_{DOC} = -21.5$ ‰.

CPD
10, 2857–2893, 2014

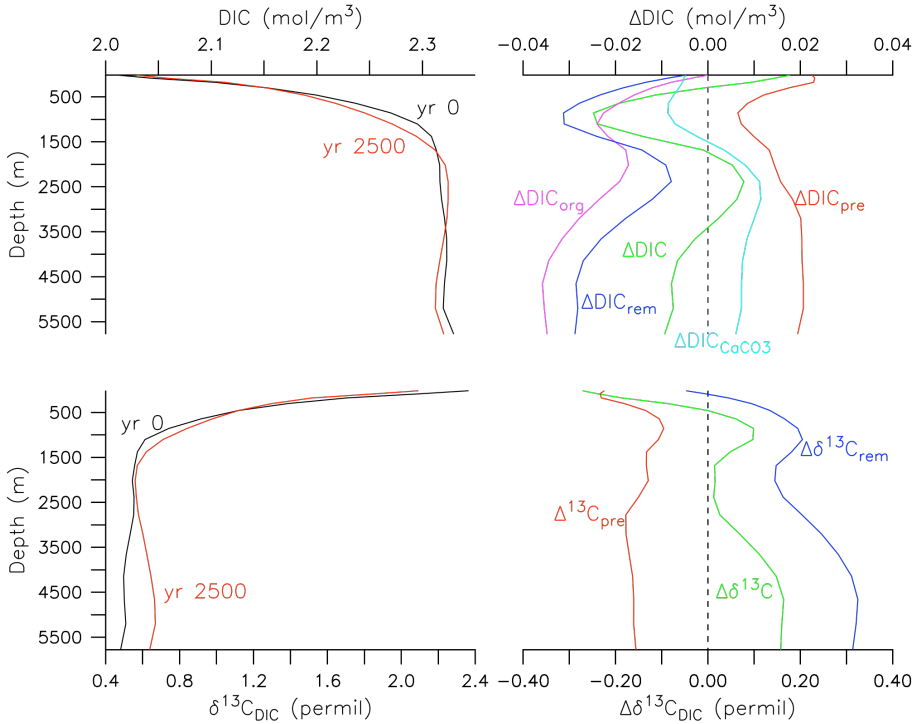

Figure 3. Vertical profiles of globally horizontally averaged ocean DIC (top left) and $\delta^{13}C$ (bottom left) at years 0 (black) and 2500 (red) of experiment FW0.15. Right panels show changes (year 2500 minus year 0) in DIC = $DIC_{pre} + DIC_{rem}$ and $\delta^{13}C = \delta^{13}C_{pre} + \delta^{13}C_{rem}$ (green) as well as individual components preformed DIC_{pre} and remineralized $DIC_{rem} = DIC_{org} + DIC_{CaCO_3}$. See Schmittner et al. (2013) for the calculation of the individual terms. The differences between the blue and green lines are due to changes in preformed DIC and $\delta^{13}C$.

CPD
10, 2857–2893, 2014

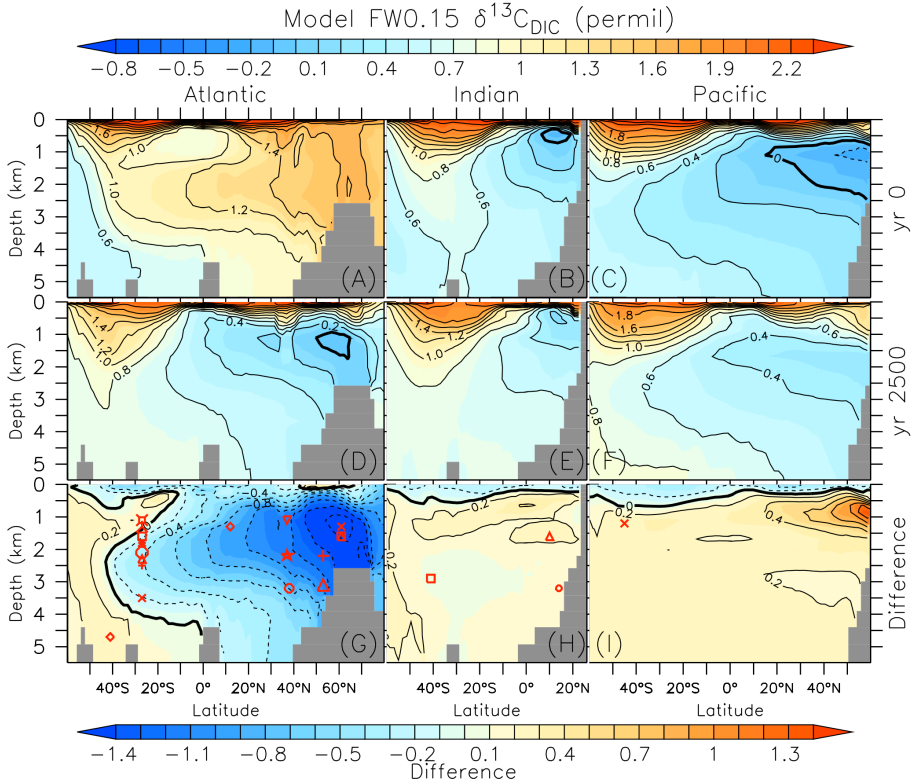

Figure 4. Zonally averaged distributions of $\delta^{13}C_{DIC}$ as a function of latitude and depth simulated by model FW0.15 in the Atlantic (left), Indian (center) and Pacific (right) ocean basins at model years 0 **(A–C)** and 2500 (**D–F**; **A–F** use top color scale), and the difference (**G–I**; bottom color scale). Red symbols in bottom panels denote locations of observations shown in Fig. 5.

CPD
10, 2857–2893, 2014

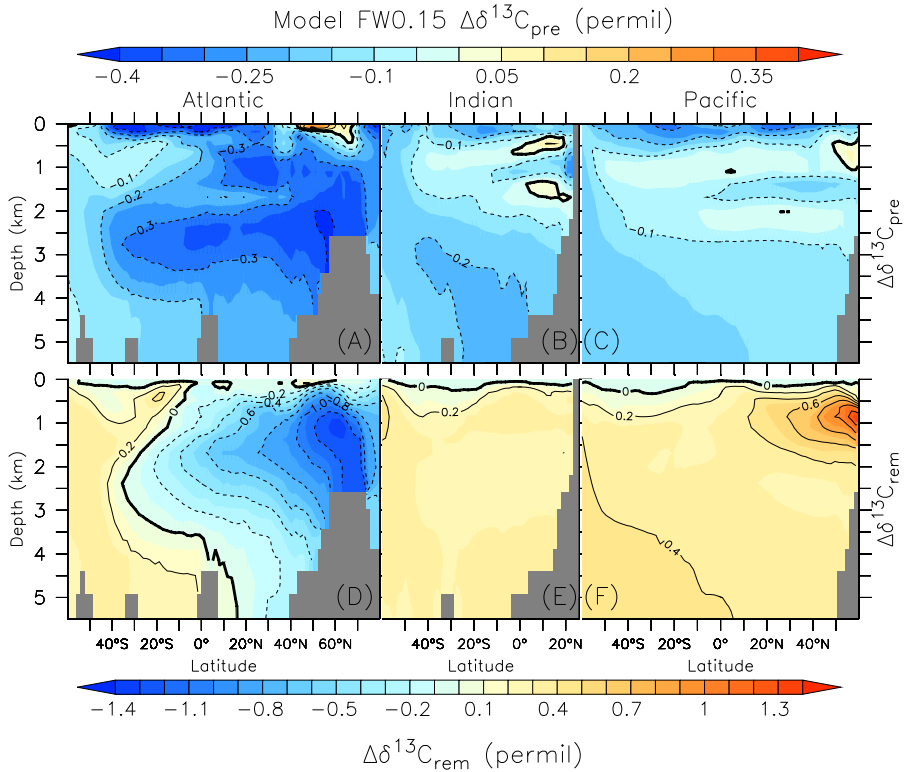

Figure 5. Impact of AMOC collapse on $\delta^{13}C_{pre}$ (top) and $\delta^{13}C_{rem}$ (bottom). Zonally averaged changes between year 2500 and year 0 of model run FW0.15 in the Atlantic (left), Indian Ocean (center), and Pacific (right). Note the different color scales and isoline differences used.

CPD
10, 2857–2893, 2014

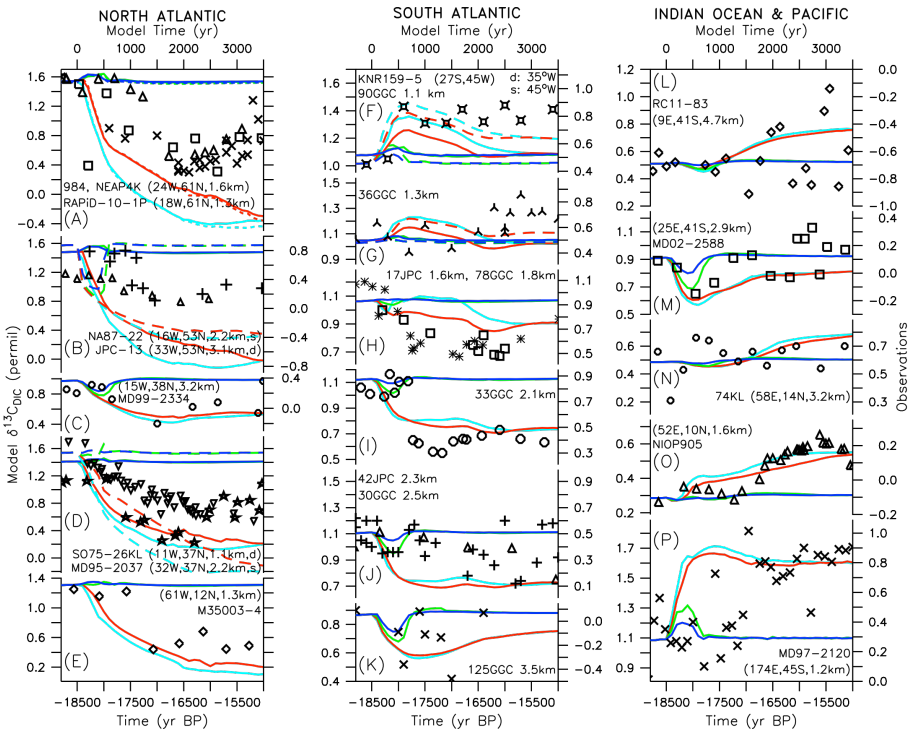

Figure 6. Comparison of simulated (lines as in Fig. 1; left and top axes) and observed (symbols as in Fig. 4; right and bottom axes) $\delta^{13}C_{DIC}$ timeseries in the North Atlantic **(A–E)**, South Atlantic **(F–L)**, Indian **(M–O)**, and Pacific **(P)** oceans. If no numbers are given on the right axis the scale is identical to the left axis. If numbers are given on the right axis the scale is different but the range (max–min) is identical to that of the left axis. Note that different ranges of the vertical axis are used for the different columns, whereas within each column they are similar.

CPD
10, 2857–2893, 2014

AMOC triggers CO_2 rise

A. Schmittner and D. C. Lund

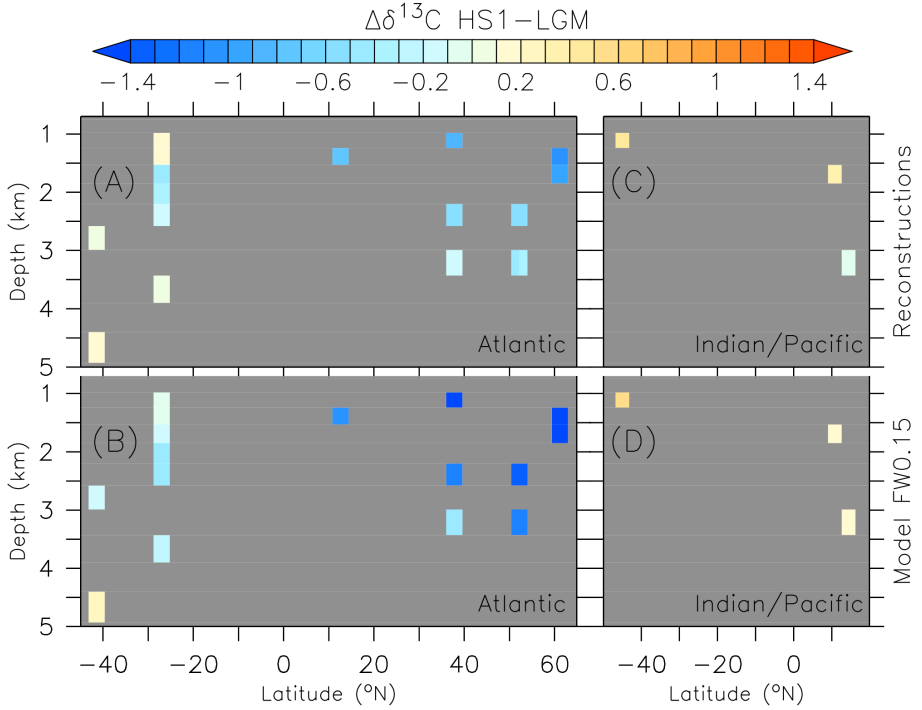

Figure 7. Heinrich Stadial 1 (16.5–15.5 ka BP) minus LGM (19.5–18.5 ka BP) difference in $\delta^{13}C_{DIC}$ in the Atlantic (left) and Indian and Pacific (right) basins from our high-resolution synthesis of reconstructions averaged on the model grid (top) compared to model FW0.15 results (bottom; averages of model years 2000 to 3000 minus averages of model years −1000 to 0.).

CPD
10, 2857–2893, 2014

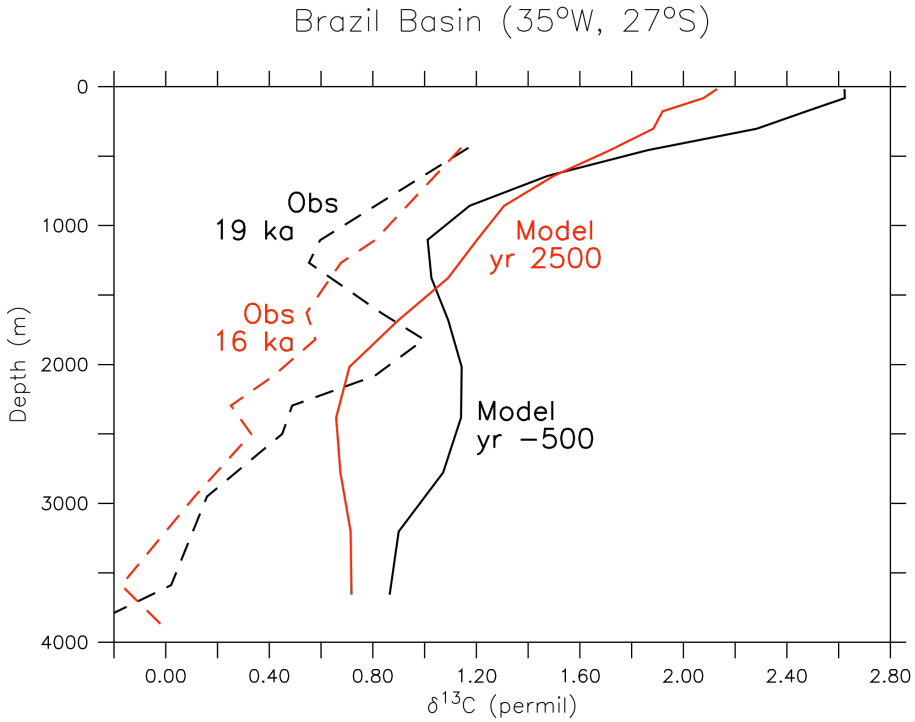

Figure 8. Simulated (solid; model FW0.15) and observed (dashed) vertical profiles of $\delta^{13}C_{DIC}$ at the Brazil Margin in the South Atlantic before (black) and after (red) the AMOC collapse. Observations show 1 ka averages of smoothed (2 ka) data. Results for model FW0.2 are very similar to FW0.15 (not shown). However, models FW0.05 and FW0.1 show almost no changes from their initial (yr −500) distribution (not shown).

CPD
10, 2857–2893, 2014

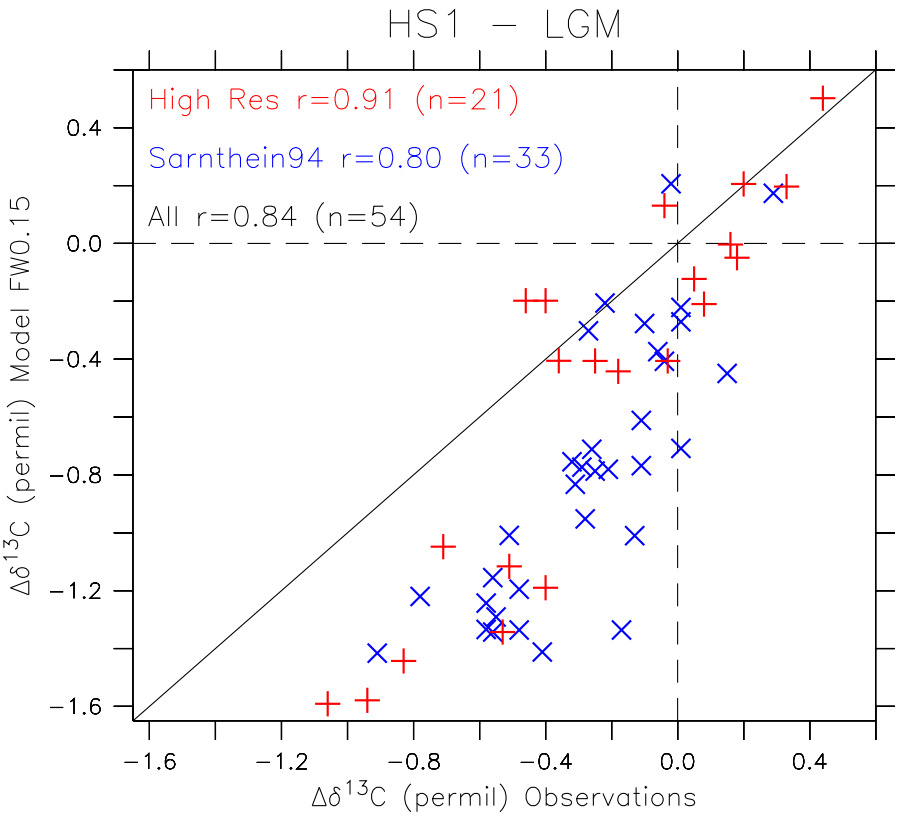

Figure 9. HS1 minus LGM change in $\delta^{13}C$ from ref (Sarnthein et al., 1994; blue) our high-resolution compilation (red) vs. changes between years 0 and 2500 predicted by model experiment FW0.15 at the same locations. The diagonal 1 : 1 line corresponds to a perfect match.

CPD
10, 2857–2893, 2014

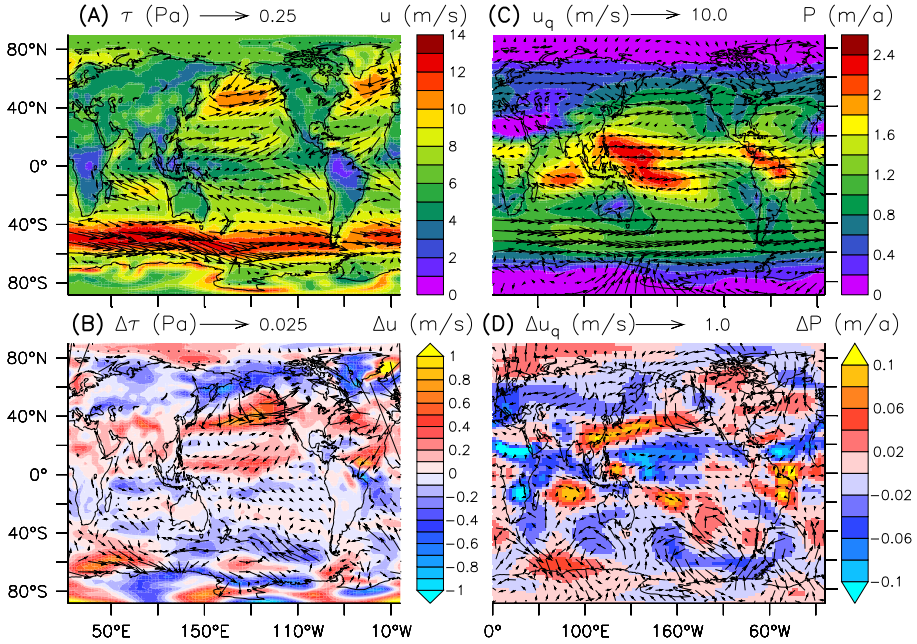

Figure 10. (A) Annual mean wind stress τ (arrows) and wind speed u (color) fields used in the control run of the UVic model. **(B)** Changes in annual mean wind stress $\Delta\tau$ and wind speed Δu derived from a hosing simulation with the OSUVic model. **(C)** and **(D)** as **(A)** and **(B)** but for moisture advection velocities u_q (arrows) and precipitation (color). Note the differences in scales between the top and bottom panels.

CPD
10, 2857–2893, 2014

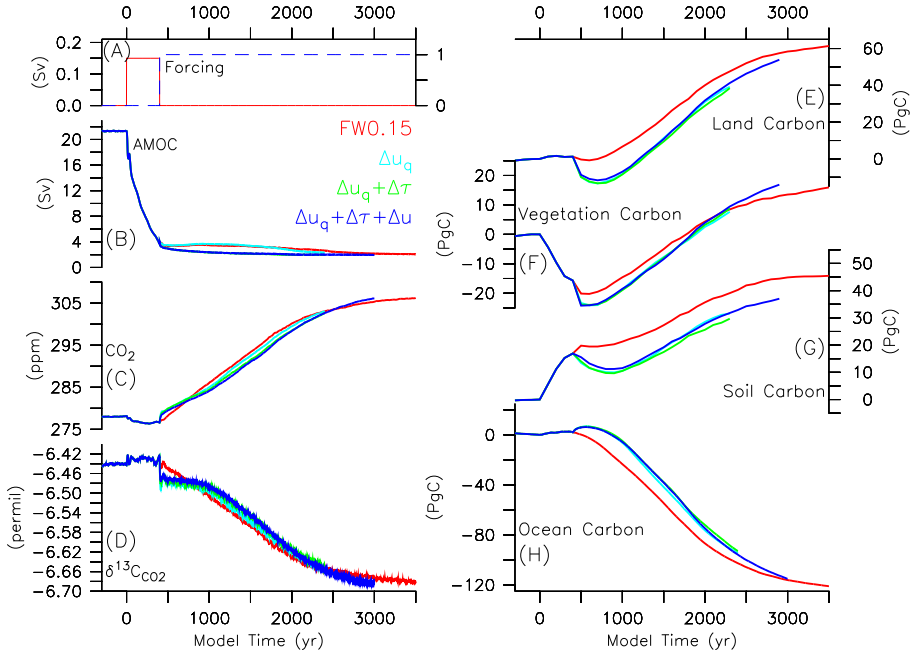

Figure 11. Sensitivity to changes in winds. Experiment FW0.15 (red) is repeated with changes in moisture advection velocities u_q (light blue), u_q plus wind stress τ (green), and $u_q + \tau$ plus wind speed u (dark blue) calculated from the OSUVic model. See Fig. 10 and text for more details.

CPD
10, 2857–2893, 2014

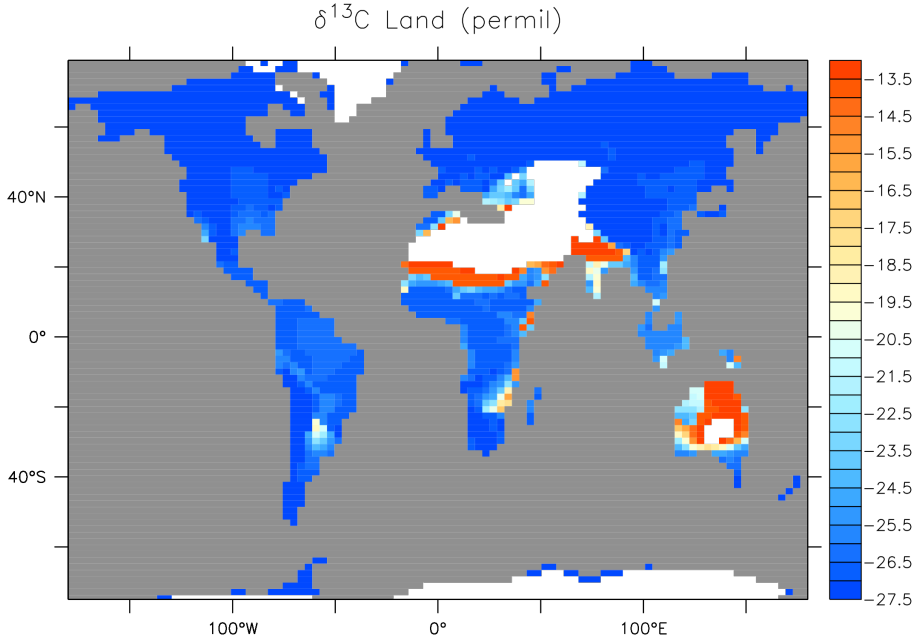

Figure 12. Simulated average pre-industrial land δ^{13}C distribution (model year 0). Each pool's (five vegetation plant functional types, PFTs, and one soil, S, carbon compartment) δ^{13}C value was weighted by its mass in calculating the average as explained in figure caption 2. Desert regions with negligible vegetation carbon ($< 10\,\mathrm{g\,m^{-2}}$) are shown in white.

CPD
10, 2857–2893, 2014